Wave Response during Hydrostatic and Geostrophic Adjustment. Part I: Transient Dynamics

JEFFREY M. CHAGNON AND PETER R. BANNON

Department of Meteorology, The Pennsylvania State University, University Park, Pennsylvania

(Manuscript received 25 September 2003, in final form 5 May 2004)

ABSTRACT

The adjustment of a compressible, stably stratified atmosphere to sources of hydrostatic and geostrophic imbalance is investigated using a linear model. Imbalance is produced by prescribed, time-dependent injections of mass, heat, or momentum that model those processes considered ''external'' to the scales of motion on which the linearization and other model assumptions are justifiable. Solutions are demonstrated in response to a localized warming characteristic of small isolated clouds, larger thunderstorms, and convective systems.

For a semi-infinite atmosphere, solutions consist of a set of vertical modes of continuously varying wavenumber, each of which contains time dependencies classified as steady, acoustic wave, and buoyancy wave contributions. Additionally, a rigid lower-boundary condition implies the existence of a discrete mode—the Lamb mode—containing only a steady and acoustic wave contribution. The forced solutions are generalized in terms of a temporal Green's function, which represents the response to an instantaneous injection.

The response to an instantaneous warming with geometry representative of a small, isolated cloud takes place in two stages. Within the first few minutes, acoustic and Lamb waves accomplish an expansion of the heated region. Within the first quarter-hour, nonhydrostatic buoyancy waves accomplish an upward displacement inside of the heated region with inflow below, outflow above, and weak subsidence on the periphery—all mainly accomplished by the lowest vertical wavenumber modes, which have the largest horizontal group speed. More complicated transient patterns of inflow aloft and outflow along the lower boundary are accomplished by higher vertical wavenumber modes. Among these is an outwardly propagating rotor along the lower boundary that effectively displaces the low-level inflow upward and outward.

A warming of 20 min duration with geometry representative of a large thunderstorm generates only a weak acoustic response in the horizontal by the Lamb waves. The amplitude of this signal increases during the onset of the heating and decreases as the heating is turned off. The lowest vertical wavenumber buoyancy waves still dominate the horizontal adjustment, and the horizontal scale of displacements is increased by an order of magnitude. Within a few hours the transient motions remove the perturbations and an approximately trivial balanced state is established.

A warming of 2 h duration with geometry representative of a large convective system generates a weak but discernible Lamb wave signal. The response to the conglomerate system is mainly hydrostatic. After several hours, the only signal in the vicinity of the heated region is that of inertia–gravity waves oscillating about a nontrivial hydrostatic and geostrophic state.

This paper is the first of two parts treating the transient dynamics of hydrostatic and geostrophic adjustment. Part II examines the potential vorticity conservation and the partitioning of total energy.

1. Introduction

Hydrostatic and geostrophic adjustment is the process by which a geophysical fluid evolves toward a state of hydrostatic and geostrophic balance. The process involves 1) the production of a localized unbalanced state, 2) the communication of the imbalance to the surrounding atmosphere by waves, and 3) the gradual establishment of a new balanced state. Atmospheric convection is a source of such imbalance. Rapid heating and the vertical redistribution of mass and momentum associated with atmospheric convection generate unbalanced mass and momentum fields. The subsequent adjustment of the larger-scale environment to the localized imbalance by the action of waves is the subject of this analysis.

The earliest investigations of geostrophic adjustment (Rossby 1937, 1938; Obukhov 1949) demonstrated the relationship between the initial and final steps of the process. Namely, these studies introduced the potential vorticity as the property of the initial condition uniquely determining the steady state. The general features of the geostrophic adjustment problem are reviewed by Blumen (1972) and Gill (1982). Buoyancy waves provide the fluid displacements necessary to adjust the distributions of mass and momentum toward a balanced state.

Corresponding author address: Jeffrey M. Chagnon, Dept. of Meteorology, The Pennsylvania State University, University Park, PA 16802.
E-mail: j.chagnon@reading.ac.uk

These waves are of great interest insofar as their interaction with the mean flow in the middle atmosphere (e.g., Holton 1983) and their role in the initiation and organization of convection (e.g., Lindzen 1974; Raymond 1976) are concerned. The complete investigation of such interactions between the waves and the environment generally requires a nonlinear model. However, the basic characteristics of the buoyancy wave spectrum, potential sources, dependence on such sources, and first-order interaction with the environment may be studied using a linear model. These issues have been the subject of many investigations of convective adjustment (e.g., Lin and Smith 1986; Raymond 1986; Bretherton and Smolarkiewicz 1989; Shutts 1994; Vadas and Fritts 2001).

A fundamental issue of the linear adjustment problem is the relationship between the characteristics of the imbalance and that of the preferentially excited waves. The vertical, horizontal, and temporal structure of a wave are given by an eigenvalue (dispersion) equation. Vadas and Fritts (2001) demonstrated that an injection of duration much longer than the characteristic period of a given buoyancy wave will not project a significant proportion of energy onto such waves. Holton et al. (2002) makes a similar argument to challenge the popular notion that the dominant gravity waves generated by convective heating have vertical wavelength equal to twice the depth of the heating. (Due to the ambiguity of the term *forcing* we use the term *injection* to denote the mechanism by which the imbalance is created.)

The overwhelming majority of studies have employed incompressible models. Fully compressible models are inherently more complicated given the existence of acoustic and Lamb waves. However, compressible numerical codes are growing in popularity (e.g., Bryan and Fritsch 2002). It is therefore necessary to analyze the potential effects of compressibility on basic atmospheric processes such as geostrophic and hydrostatic adjustment. Chagnon and Bannon (2001) demonstrated that the steady-state solutions in anelastic and other sound filtering models exhibit significant differences from a fully compressible model. Bannon (1995) theorizes that acoustic waves can provide the vertical displacements necessary to adjust a heated cloud layer toward hydrostatic balance. In a fully compressible numerical simulation of an isolated convective cloud, Nicholls and Pielke (2000) identified a Lamb wave propagating away from the cloud containing internal and gravitational potential energy approximately equal to the total latent heating within the cloud.

This paper investigates the acoustic and buoyancy wave response to rapid, localized sources of hydrostatic and geostrophic imbalance. Our goal is to describe the response according to several regimes dominated by either acoustic waves, nonhydrostatic buoyancy waves, Lamb waves, nonrotating hydrostatic buoyancy waves, or rotating hydrostatic buoyancy waves. The association of the various response regimes to a given imbalance generation mechanism will be examined in terms of the spatial and temporal detail of the injection. The investigation consists of two parts: Part I presents the time-dependent solution of a linear model in order to illustrate the various response regimes. Part II (Chagnon and Bannon 2005) examines the potential vorticity and total energy of the model, the latter of which is partitioned among the various wave classes. Motivated by Nicholls and Pielke (2000) and Chagnon and Bannon (2001), this analysis will consider the adjustment of a fully compressible atmosphere with a rigid lower boundary which contains Lamb and acoustic waves. We seek to determine under what circumstances the effects of compressibility may be significant to hydrostatic and geostrophic adjustment. Although the mathematical solutions are presented following general injections of mass, momentum, and heat, the specific solutions are demonstrated following only a heating. A subsequent article will apply these mathematical solutions in order to compare the adjustment to injections of different type (i.e., mass, momentum, and heat).

Part I of this paper is organized as follows. Section 2 introduces the mathematical model. Section 3 presents the solution of the model. The structure of solutions to the homogeneous problem is shown to consist of distinct acoustic wave, Lamb wave, buoyancy wave, and steady classes. The solutions to the nonhomogeneous problem are expressed in terms of a temporal Green's function whose structure resembles that of the homogeneous solution. Section 4 demonstrates the solution of the model subject to external heating of varying spatial and temporal scale. Section 5 discusses the results of the previous sections and assesses the significance of compressible waves in models of hydrostatic and geostrophic adjustment.

2. The model

Governing equations

The model framework for this investigation is a compressible, dry, inviscid, ideal gas in Cartesian coordinates that is assumed invariant in the y direction and is linearized on an f plane about an isothermal, resting base state. This highly idealized model is chosen for its tractability while maintaining many essential physical characteristics of midlatitude, large-scale atmospheric flows. The nonhomogeneous terms in the model represent injections of mass, momentum, and heat by the smaller-scale and/or smaller-amplitude disturbances. The governing equations are

$$\rho_s \frac{\partial u'}{\partial t} = -\frac{\partial p'}{\partial x} + \rho_s f v' + \rho_s \dot{u}, \qquad (2.1a)$$

$$\rho_s \frac{\partial v'}{\partial t} = -\rho_s f u' + \rho_s \dot{v}, \tag{2.1b}$$

$$\rho_s \frac{\partial w'}{\partial t} = -\frac{\partial p'}{\partial z} - \rho' g + \rho_s \dot{w}, \tag{2.1c}$$

$$\frac{\partial \theta'}{\partial t} + w' \frac{\partial \theta_s}{\partial z} = \dot{\Theta}, \tag{2.1d}$$

$$\frac{\partial \rho'}{\partial t} + \frac{\partial}{\partial x}(\rho_s u') + \frac{\partial}{\partial z}(\rho_s w') = \dot{\rho}, \tag{2.1e}$$

$$\frac{\theta'}{\theta_s} = \frac{p'}{\gamma p_s} - \frac{\rho'}{\rho_s}, \tag{2.1f}$$

where g is the acceleration due to gravity, f is the constant Coriolis parameter, and $\gamma = c_p/c_v = 1.4$ is the ratio of specific heat capacities. A subscript s denotes a static, base-state quantity, and a superscript prime denotes a perturbation from the base state. The base-state quantities are assumed to be functions of height only [e.g., $p(x, y, z, t) = p_s(z) + p'(x, y, z, t)$]. The isothermal, hydrostatic base state is described by

$$T_s = T_*, \qquad p_s = p_* \exp(-z/H_s),$$
$$\rho_s = \rho_* \exp(-z/H_s), \qquad \theta_s = \theta_* \exp(\kappa z/H_s), \tag{2.2}$$

where T_*, p_*, θ_*, and ρ_* are constants satisfying the ideal gas law and Poisson's relation. Here, $\kappa = R_d/c_p$, and $H_s = R_d T_s/g$ is the density-scale height in an isothermal atmosphere. The rates of injection of x momentum, y momentum, z momentum, potential temperature, and density are represented by $\dot{u}$, $\dot{v}$, $\dot{w}$, $\dot{\Theta}$, and $\dot{\rho}$, respectively, and have arbitrary spatial and temporal structure.

The model equations are simplified by the introduction of ''field variables,'' which remove any height dependence of the coefficients in the system of partial differential equations (Eckart 1960). The field variables are defined as

$$\mathbf{U} = \rho_s^{1/2}\mathbf{u}', \qquad P = \frac{1}{\rho_s^{1/2}} p', \qquad R = \frac{1}{\rho_s^{1/2}} \rho',$$
$$S = \frac{\rho_s^{1/2}}{\theta_s} \theta'. \tag{2.3}$$

Applying (2.3) to (2.1) we obtain the simplified system of equations:

$$\frac{\partial \boldsymbol{\chi}}{\partial t} + \mathbf{A}\boldsymbol{\chi} = \mathbf{F}, \tag{2.4}$$

where the solution state vector is $\boldsymbol{\chi}^{\mathrm{T}} = (U, V, W, S, P)$, the matrix operator $\mathbf{A}$ is given by

$$\mathbf{A} = \begin{bmatrix} 0 & -f & 0 & 0 & \frac{\partial}{\partial x} \\ f & 0 & 0 & 0 & 0 \\ 0 & 0 & 0 & -g & \frac{\partial}{\partial z} + \Gamma \\ 0 & 0 & \frac{\kappa}{H_s} & 0 & 0 \\ c_s^2 \frac{\partial}{\partial x} & 0 & c_s^2\left(\frac{\partial}{\partial z} - \Gamma\right) & 0 & 0 \end{bmatrix}, \tag{2.5}$$

where Eckart's (1960) vertical expansion parameter is defined as

$$\Gamma \equiv \left(\frac{1}{\gamma} - \frac{1}{2}\right)\frac{1}{H_s}, \tag{2.6}$$

and the injection vector is $\mathbf{F}^{\mathrm{T}} = (\dot{U}, \dot{V}, \dot{W}, \dot{S}, \dot{P})$ where the mass-weighted injection terms are given by

$$(\dot{U}, \dot{V}, \dot{W}) = \rho_s^{1/2}(\dot{u}, \dot{v}, \dot{w}), \qquad \dot{R} = \rho_s^{-1/2}\dot{\rho},$$
$$\dot{S} = \frac{\rho_s^{1/2}}{\theta_s}\dot{\Theta}, \qquad \dot{P} = c_s^2(\dot{S} + \dot{R}), \tag{2.7}$$

where $c_s = (\gamma R_d T_s)^{1/2}$ is the adiabatic speed of sound. The density field may be obtained via the transformed Poisson's relation $P = c_s^2 (S + R)$. The horizontal dependence of the fields is represented by a Fourier transform,

$$\phi_k(k) = \int_{-\infty}^{\infty} \phi(x) e^{-ikx}\, dx,$$
$$\phi(x) = \frac{1}{2\pi}\int_{-\infty}^{\infty} \phi_k(k) e^{ikx}\, dk, \tag{2.8}$$

where $i = \sqrt{-1}$. All of the subsequent analysis in this article is performed in Fourier transform space (except the solutions of section 4, which are presented in ''physical space''). In order to keep the notation as simple and clean as possible, we will not denote the Fourier transform explicitly by a subscript k. Under the transform (2.8) the operator $\mathbf{A}$ becomes

$$\mathbf{A} = \begin{bmatrix} 0 & -f & 0 & 0 & ik \\ f & 0 & 0 & 0 & 0 \\ 0 & 0 & 0 & -g & \frac{\partial}{\partial z} + \Gamma \\ 0 & 0 & \frac{\kappa}{H_s} & 0 & 0 \\ ikc_s^2 & 0 & c_s^2\left(\frac{\partial}{\partial z} - \Gamma\right) & 0 & 0 \end{bmatrix}.$$

Our goal is to solve (2.4) subject to the initial condition that all of the fields are undisturbed for $t < 0$,

$$\boldsymbol{\chi} = \mathbf{0}, \qquad t < 0, \tag{2.9}$$

and the boundary conditions that $w = 0$ at heights $z = 0, 2D$,

$$\left[\left(\frac{\partial}{\partial z} + \Gamma\right)U, \left(\frac{\partial}{\partial z} + \Gamma\right)V, W, S, \left(\frac{\partial}{\partial z} + \Gamma\right)P\right] = \mathbf{0}^{\mathrm{T}}, \quad z = 0, 2D. \tag{2.10}$$

The application of the homogeneous boundary condition (2.10) is valid when the injection is zero on the boundaries. The structure of the solutions in the semi-infinite atmosphere is identical to those in a finite atmosphere in the limit as $D \to \infty$. The rigid lower-boundary condition implies the existence of a boundary wave (i.e., a wave with maximum amplitude along the boundary whose existence is owed to the presence of the boundary), which we identify as the Lamb wave (Lamb 1932, section 311a). We need not worry about a spurious boundary wave corresponding to the rigid upper boundary, because $g > N_s c_s$ (Iga 2001) where $N_s = [(g/\theta_s)d\theta_s/dz]^{1/2}$ is the buoyancy frequency. The Lamb wave is a hydrostatic, adiabatic, horizontally propagating wave that responds to changes in the column pressure that act against the rigid lower boundary.

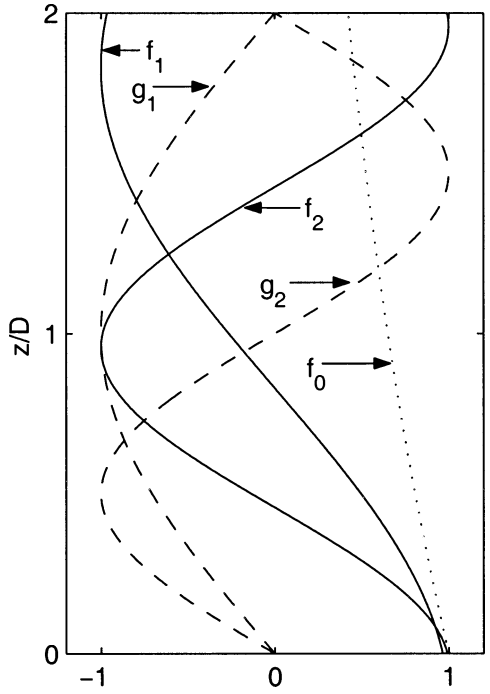

FIG. 1. Vertical profiles of the first three vertical basis functions. The pressure and horizontal velocity fields are described by f_n. The potential temperature and vertical velocity fields are described by g_n. The Lamb mode is f_0. Here, $D = 15$ km, $H_s = 7.47$ km.

3. Solution

a. Homogeneous solutions

Examination of the homogeneous solutions of (2.4) reveals the fundamental dynamic components of the adjustment process. We look for separable solutions: $\boldsymbol{\chi}^{\mathrm{T}} = (U_n(t)f_n(z), V_n(t)f_n(z), W_n(t)g_n(z), S_n(t)g_n(z), P_n(t)f_n(z))$. Two distinct vertical structure functions f_n and g_n are sought to satisfy the distinct vertical boundary conditions in (2.10). For W and S we require $g_n = 0$ on the boundaries, and for U, V, and P we require $[d/dz + \Gamma]f_n = 0$ on the boundaries. Substituting the separable form of $\boldsymbol{\chi}$ into the homogeneous form of (2.4) implies that the vertical structure functions must satisfy

$$f_n''(z) + m^2 f_n(z) = 0, \tag{3.1a}$$

$$g_n''(z) + m^2 g_n(z) = 0, \tag{3.1b}$$

where the vertical decay scale m is a constant of proportionality between the vertical and temporal structure equations. The simple form of (3.1) gives way to more complicated forms when the base state is spatially varying (e.g., Fritts and Yuan 1989). Because (3.1) are Sturm–Liouville boundary-value problems, the collection of linearly independent solutions forms orthogonal basis sets between the boundaries. These sets are given by

$$f_0, f_1, f_2, f_3, \ldots; \qquad f_0 = e^{-\Gamma z} \tag{3.2a}$$

where

$$f_n = m\cos(mz) - \Gamma\sin(mz), \qquad m = \frac{n\pi}{2D},$$

and

$$g_0(=0), g_1, g_2, g_3, \ldots, \tag{3.2b}$$

where

$$g_n = \left(\frac{d}{dz} + \Gamma\right)f_n = -(m^2 + \Gamma^2)\sin(mz).$$

Here and elsewhere, *mode* refers to a specific spatial structure given by the set (3.2) along with the Fourier transform in x. The zeroth vertical mode f_0 is the Lamb mode that is hydrostatic and contains zero entropy. Figure 1 plots the profile of the first three modes in (3.2). The modes describing the vertical velocity are zero on the boundaries. With the exception of the Lamb mode, the modes describing the pressure have equal magnitude on the upper and lower boundary but alternate between the same and opposite signs (with increasing n). The solution may be written as a linear combination of the vertical basis functions,

$$\boldsymbol{\chi}^{\mathrm{T}} = \sum_{n=0}^{\infty}(U_n f_n, V_n f_n, W_n g_n, S_n g_n, P_n f_n). \tag{3.3}$$

In the semi-infinite limit, the discrete sum (3.3) may be replaced by an integral over continuously varying wavenumber m. The time dependence of the nth mode must satisfy

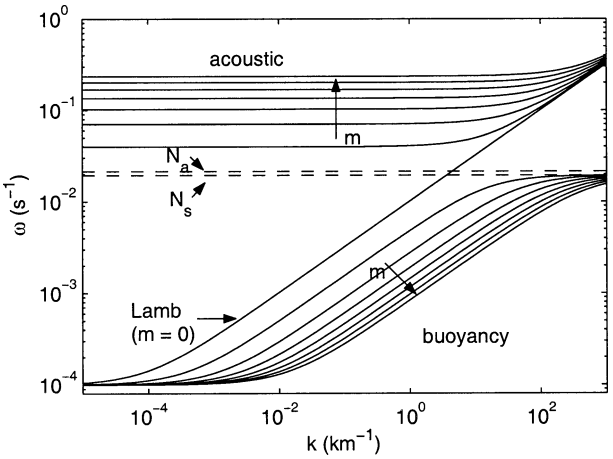

FIG. 2. Dispersion curves for the first eight vertical modes m as a function of the horizontal wavenumber k. Here, $T_s = 255$ K and the domain depth is $2D = 30$ km. The acoustic cutoff frequency is $N_a = 0.0214\ \mathrm{s}^{-1}$, the maximum buoyancy frequency is $N_s = 0.0194\ \mathrm{s}^{-1}$, and $f = 10^{-4}\ \mathrm{s}^{-1}$.

$$\frac{d\boldsymbol{\chi}_n}{dt} + \mathbf{A}_n\boldsymbol{\chi}_n = 0, \tag{3.4}$$

where $\boldsymbol{\chi}_n^{\mathrm{T}} = (U_n, V_n, W_n, S_n, P_n)$, and

$$\mathbf{A}_n = \begin{bmatrix} 0 & -f & 0 & 0 & ik \\ f & 0 & 0 & 0 & 0 \\ 0 & 0 & 0 & -g & 1 \\ 0 & 0 & \dfrac{\kappa}{H_s} & 0 & 0 \\ ikc_s^2 & 0 & -c_s^2(m^2 + \Gamma^2) & 0 & 0 \end{bmatrix}. \tag{3.5}$$

The eigenvalues of $\mathbf{A}_n$ are the five roots of the dispersion relation

$$\lambda_i(\lambda_i^4 + \alpha\lambda_i^2 + \beta) = 0, \tag{3.6}$$

where

$$\alpha = (c_s^2k^2 + f^2) + c_s^2(\Gamma^2 + m^2) + N_s^2,$$

$$\beta = c_s^2f^2(\Gamma^2 + m^2) + N_s^2(c_s^2k^2 + f^2).$$

Solutions of (3.4) have temporal dependence $e^{-\lambda t}$, as will be demonstrated later. The eigenvalue $\lambda_1 = 0$ corresponds to a steady solution. The four other eigenvalues are complex: $\lambda_{2,3} = \pm i\omega_a$, $\lambda_{4,5} = \pm i\omega_b$ where ω_a and ω_b are frequencies characteristic of acoustic and buoyancy waves, respectively, and are given by the nontrivial solution of (3.6), $\omega_{a,b} = [\alpha \pm (\alpha^2 - 4\beta)^{1/2}]^{1/2}/4$. (Note that these frequencies are real provided $N_s^2 > f^2$). Figure 2 presents the dependence of the frequencies on the horizontal k and vertical m wavenumbers. Equation (3.6) and Fig. 2 suggest three classes of time dependence for each mode: steady, acoustic wave, and buoyancy wave. Here and elsewhere, *class* refers to these time dependencies. The Lamb mode contains only two classes: steady and acoustic wave (i.e., the Lamb wave). The frequency of buoyancy cannot exceed N_s, whereas the acoustic waves have lower bound $N_a = c_s/2H_s$, the acoustic cutoff frequency. The lower bound on all oscillations is twice the angular velocity of the coordinate frame f. A similar diagram exists in Gill (1982, his Fig. 6.18) for the nonrotating case ($f = 0$), but is provided here as a convenient reference for the interpretation of the solutions presented in section 4 and the energetics of part II.

The eigenvectors of $\mathbf{A}_n$ are

$$\mathbf{e}_i^{\mathrm{T}} = P_n\left(\frac{ik\lambda_i}{\lambda_i^2 + f^2}, \frac{ikf}{\lambda_i^2 + f^2}, \frac{\lambda_i}{\lambda_i^2 + N_s^2}, \frac{\kappa/H_s}{\lambda_i^2 + N_s^2}, 1\right). \tag{3.7}$$

Let $\mathbf{E}_n$ be the matrix whose column's vectors are the eigenvectors (3.7),

$$\mathbf{E}_n \equiv [\mathbf{e}_1 : \mathbf{e}_2 : \mathbf{e}_3 : \mathbf{e}_4 : \mathbf{e}_5]_n. \tag{3.8}$$

The matrix $\mathbf{E}_n^{-1}\mathbf{A}_n\mathbf{E}_n$ is the diagonal matrix containing the eigenvalues λ_i. Transforming $\boldsymbol{\chi}_n = \mathbf{E}_n\boldsymbol{\psi}_n$ implies that $d\boldsymbol{\psi}_n/dt = -\mathbf{E}_n^{-1}\mathbf{A}_n\mathbf{E}_n\boldsymbol{\psi}_n$. The ith element of the transformed solution vector, $\boldsymbol{\psi}_n$, is therefore $\psi_i = C_i \exp(-\lambda_i t)$ where C_i is constant. That is, the five elements of the transformed solution vector correspond to steady, acoustic, and buoyancy contributions. The solution vector is therefore given by

$$\boldsymbol{\chi}_n = \begin{pmatrix} 0 & \dfrac{-f\omega_a}{f^2 - \omega_a^2} & \dfrac{k\omega_a}{f^2 - \omega_a^2} & \dfrac{-k\omega_b}{f^2 - \omega_b^2} & \dfrac{k\omega_b}{f^2 - \omega_b^2} \\ \dfrac{ik}{f} & \dfrac{ikf}{f^2 - \omega_a^2} & \dfrac{ikf}{f^2 - \omega_a^2} & \dfrac{ikf}{f^2 - \omega_b^2} & \dfrac{ikf}{f^2 - \omega_b^2} \\ 0 & \dfrac{i\omega_a}{N_s^2 - \omega_a^2} & \dfrac{-i\omega_a}{N_s^2 - \omega_a^2} & \dfrac{i\omega_b}{N_s^2 - \omega_b^2} & \dfrac{-i\omega_b}{N_s^2 - \omega_b^2} \\ \dfrac{1}{g} & \dfrac{\kappa/H_s}{N_s^2 - \omega_a^2} & \dfrac{\kappa/H_s}{N_s^2 - \omega_a^2} & \dfrac{\kappa/H_s}{N_s^2 - \omega_b^2} & \dfrac{\kappa/H_s}{N_s^2 - \omega_b^2} \\ 1 & 1 & 1 & 1 & 1 \end{pmatrix}_n \times \begin{pmatrix} C_1 \\ C_2e^{-i\omega_a t} \\ C_3e^{i\omega_a t} \\ C_4e^{-i\omega_b t} \\ C_5e^{i\omega_b t} \end{pmatrix}_n. \tag{3.9}$$

The constants C_i are determined by the initial conditions. The column vectors of $\mathbf{E}_n$ describe the structure of the steady, acoustic, and buoyancy contributions to the homogeneous solution. The first column vector gives the structure of the hydrostatic and geostrophic contribution, which contains zero contribution from the U and W fields. The next four column vectors indicate the structure of the acoustic and buoyancy waves. A 90° temporal phase difference exists between the U, W and P, V, S fields. A 90° horizontal phase difference exists

between the *U, V* and *P, W, S* fields. The dependence of the frequency ω on the vertical m and horizontal k structure of the mode (i.e., the dispersion relation) determines the properties of the group and phase velocities. Specifically, these velocities are spatially orthogonal for the buoyancy waves and parallel for the acoustic waves.

b. Response to external injection

We seek the solution to the nonhomogeneous form of (2.4) using the properties of the homogeneous solutions. If the injection vector is expanded about the vertical basis functions,

$$\mathbf{F}^{\mathrm{T}} = \sigma_t \sigma_k \sum_{n=0}^{\infty} (s_1 f_n,\ s_2 f_n,\ s_3 g_n,\ s_4 g_n,\ s_5 f_n), \quad (3.10)$$

where σ_t is the time dependence of the injection, σ_k is the Fourier transformed horizontal dependence of the injection, and s_i is the projection of the ith component of the injection vector onto the appropriate vertical basis function, then (2.4) may be written as

$$\frac{d\boldsymbol{\chi}_n}{dt} + \mathbf{A}_n \boldsymbol{\chi}_n = \mathbf{F}_n, \quad (3.11)$$

where $\mathbf{F}_n^{\mathrm{T}} = \sigma_t \sigma_k (s_1, s_2, s_3, s_4, s_5)_n$. The particular solution of (3.11) may be expressed in terms of the temporal Green's function $\hat{\boldsymbol{\chi}}_n$,

$$\boldsymbol{\chi}_n(t) = \int_0^t \hat{\boldsymbol{\chi}}_n(t - t')\sigma_t(t')\, dt'. \quad (3.12)$$

The Green's function is the particular solution of

$$\frac{d\hat{\boldsymbol{\chi}}_n}{\mathbf{dt}} + \mathbf{A}_n \hat{\boldsymbol{\chi}}_n = \hat{\mathbf{F}}_n, \quad (3.13)$$

where $\hat{\mathbf{F}}_n^{\mathrm{T}} = \delta(t)\sigma_k(s_1, s_2, s_3, s_4, s_5)_n$. We may look for a solution $\hat{\boldsymbol{\chi}}_n$ of (3.13) resembling that of the homogeneous problem given by (3.9), $\hat{\boldsymbol{\chi}}_n = \mathbf{E}_n \boldsymbol{\psi}_n$. The conditions on the constants C_i of $\boldsymbol{\psi}_n$ are found by integrating (3.13) about an infinitesimal region in time containing $t = 0$ and applying the initial condition that $\hat{\boldsymbol{\chi}}_n = \mathbf{0}$ for $t < 0$. The constants must therefore satisfy the linear system given by

$$\lim_{t \to 0^+} (\mathbf{E}_n \boldsymbol{\psi}_n) = \lim_{\varepsilon \to 0} \int_{-\varepsilon}^{\varepsilon} \hat{\mathbf{F}}_n\, dt, \quad (3.14)$$

which may be solved readily upon inverting the eigenvector matrix $\mathbf{E}_n$. The appendix provides the solution of (3.14). Although the form of the coefficients given by (A1)–(A5) is not extremely elegant, we may still recognize some physically meaningful properties. For example, the coefficient of the steady contribution C_1 is zero when the injection is of x velocity or vertical velocity, neither of which may generate potential vorticity (see part II, section 2). For these same injections $C_2 = -C_3$, $C_4 = -C_5$ which implies that the pressure field varies like a sine in time and is initially zero. For an injection of y velocity $C_2 = C_3$, $C_4 = C_5$ which implies pressure varies like a cosine in time that is exactly offset by the steady contribution initially. For an injection of heat or mass the solution contains a steady state $C_1 \neq 0$ and varies like a cosine in time with nonzero initial perturbation.

The temporal convolution (3.12) may be expressed as $\boldsymbol{\chi}_n(t) = \mathbf{E}_n \mathbf{G}_n(t)$ where the ith element of $\mathbf{G}_n(t)$ is $G_{n,i} = c_i(t) \exp(i\omega_i t)$ with

$$c_i(t) = C_i \int_0^t e^{-i\omega_i t'}\, \sigma_t(t')\, dt'. \quad (3.15)$$

The kernel functions $C_i \exp(-i\omega_i t)$ in (3.15) depend on the nature of the eigenvalue spectrum and the spatial projection of the injection onto the modes. The time-dependent coefficients, given by (3.15), may be calculated readily given the temporal structure of the injection σ_t. The resulting solution in spectral space must be summed over the vertical basis functions and inverse Fourier transformed to obtain the solution in physical space. The field variables may then be transformed via (2.3) to remove the mass weightings of the basic state.

4. Response to heating

The solution presented in the previous section consists potentially of a broad spectrum of waves that accomplish a broad range of motions. The response to any given injection is likely to excite preferentially a specific region of this spectrum. We therefore expect the characteristics of the response to depend on the spatial and temporal detail of the injection. The following series of experiments examines this dependence and demonstrates several stages of the adjustment process. Let us consider the response to an injection of heat of the form

$$\dot{\Theta} = \frac{2\Delta\theta}{\tau}\left[\frac{1}{1 + (x/a)^2}\right] H^*(z,\ d_g,\ d + d_g) \times \sin^2\left[\frac{\pi}{d}(z - d_g)\right] H^*(t,\ 0,\ \tau)\, \sin^2\left(\frac{\pi t}{\tau}\right), \quad (4.1)$$

where a is the heating half-width, d is the heating depth, d_g is the heating elevation, τ is the heating duration, $\Delta\theta$ is the heating amplitude, $H^*(x, x_1, x_2) = H(x - x_1) - H(x - x_2)$ is the top-hat function between $x = x_1$ and $x = x_2$ and H is the Heaviside step function. Figure 3 presents the spatial structure of this heating. The heating aspect ratio $\delta = d/2a$ and the duration τ are varied through a range of scales representing that of individual clouds to organized convective systems. For each of the experiments, the base state is described by $T_* = 255$ K, $p_* = 1000$ mb, $\rho_* = 1.37$ kg m^{-3}, $N_s = .0194$ s^{-1}, $H_s = 7.48$ km, $c_s = 320$ m s^{-1}, $f = 10^{-4}$ s^{-1}, and the heating amplitude is $\Delta\theta = 1$ K. The base state tem-

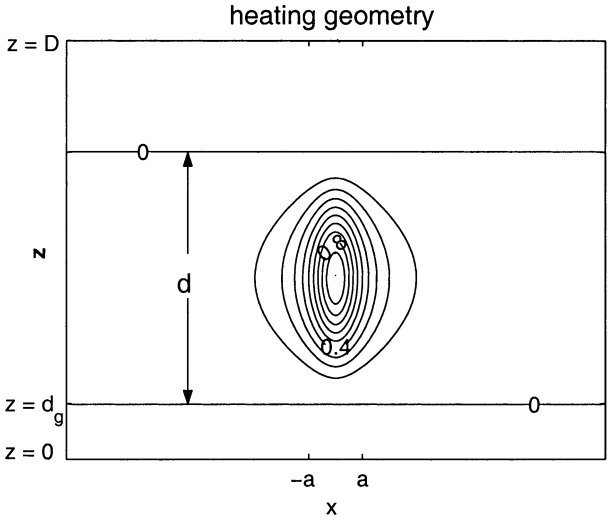

FIG. 3. Geometry of the heat injection, demonstrating the heating half-width a, the depth d, the elevation d_g, and domain half-depth D. A rigid upper boundary is placed at $z = 2D$.

perature is chosen such that the scale height and sound speed are representative of the middle troposphere. The base-state pressure is chosen such that the total column mass is of a typical atmospheric value. As a note of caution, it is important to recognize that the buoyancy frequency N_s is about twice as large as a typical tropospheric value ($\sim 0.01\ s^{-1}$) and is therefore more appropriate for the stratosphere. This is an unfortunate shortcoming of the isothermal base state that cannot be avoided without the specification of extraordinary basic-state temperature. In order for the isothermal basic state to have $N_s = 0.01\ s^{-1}$, the temperature would have to be $T_* = 956$ K. The consequence of the exaggerated buoyancy frequency is a two-fold decrease in the buoyancy period. The nonhydrostatic buoyancy wave response demonstrated in the following experiments will therefore occur more rapidly than in the natural troposphere. In each experiment 512 horizontal modes and 51 vertical modes are used to construct the solutions, and the domain depth is taken to be several scale heights, $2D = 30$ km. A Lanczos smoother (Arfken 1970) is applied to improve the convergence properties of derivatives of Fourier transformed variables.

A useful quantity for examining the characteristics of the response is the parcel displacement. The time-dependent parcel displacement fields (Δx, Δz) are found by integrating the y momentum (2.1b) and heat (2.1d) equations in time to yield,

$$\Delta x(t) = -\frac{1}{f}\left(v' - \int_{t_0<0}^{t} \dot{v}\, dt\right),$$

$$\Delta z(t) = -\frac{g}{\theta_s N_s^2}\left(\theta' - \int_{t_0<0}^{t} \dot{\Theta}\, dt\right). \qquad (4.2)$$

Chagnon and Bannon (2001) discuss the salient features of this net displacement field at $t \to \infty$. The mechanism by which the net upper-level outflow, lower-level inflow, and upward displacement of the heated column is achieved is demonstrated by observing the time-dependent evolution of the displacement fields. In the following three experiments, the size and duration of the heat injection are chosen to represent cumulus-scale, mesoscale, and intermediate-scale injections. It should be noted that the geometry of the heating (4.1) is essentially two-dimensional, or ''horizontally extended.'' This does not mean they are appropriate for modeling the extended weather systems in nature, such as squall lines and fronts, because the evolution of such natural phenomena depends strongly on the shear in the basic state. The following experiments are more appropriate to adjustment within low-shear environments. The constraining assumption of horizontal invariance will mainly lead to an underestimate of the decay of energy density within the two-dimensional wave groups.

a. Cumulus-scale heating (tall aspect ratio, short duration)

In the first experiment, we let $a = 2$ km, $d = 5$ km, $d_g = 1$ km, and $\tau \to 0$ such that the heating is impulsive (i.e., Dirac delta function in time) with aspect ratio of $\delta = 1.25$. Although the instantaneous heating is not physical, the solution is informative since it represents the temporal Green's function solution $\hat{\boldsymbol{\chi}}$, which emphasizes the response by the highest frequency waves. The characteristics of such an injection are most representative of a small isolated convective cloud.

Figure 4 presents the time-dependent displacement field in the first minute following the heat injection. The initial adjustment is dominated by acoustic waves generated in the regions of heating gradient. The displacements occur in the direction of energy propagation and accomplish a net expansion of the heated region. The portion of the acoustic signal that propagates horizontally with a pressure maximum located along the lower boundary is the Lamb wave.

Figure 5 presents temporal cross sections of the pressure field. During the acoustic stage, the initial pressure perturbation of 307 Pa is drastically reduced in amplitude. Two distinct vertically propagating wave groups are evident in Fig. 5a emanating from the upper and lower halves of the heated region. The leading edge of each group is a large high pressure perturbation, followed by a region of smaller-amplitude negative perturbation. The approach of the upward propagating high (low) pressure perturbation is associated with upward (downward) acceleration. The downward propagating wave group is reflected off the lower boundary, indicated by a positive pressure perturbation emerging along the lower boundary between $t \approx 5$ s and $t \approx 15$ s. The vertical profile of pressure perturbation remaining after these waves have left the heated region (i.e., the profile along the right-hand edge of Fig. 5a) differs qualita-

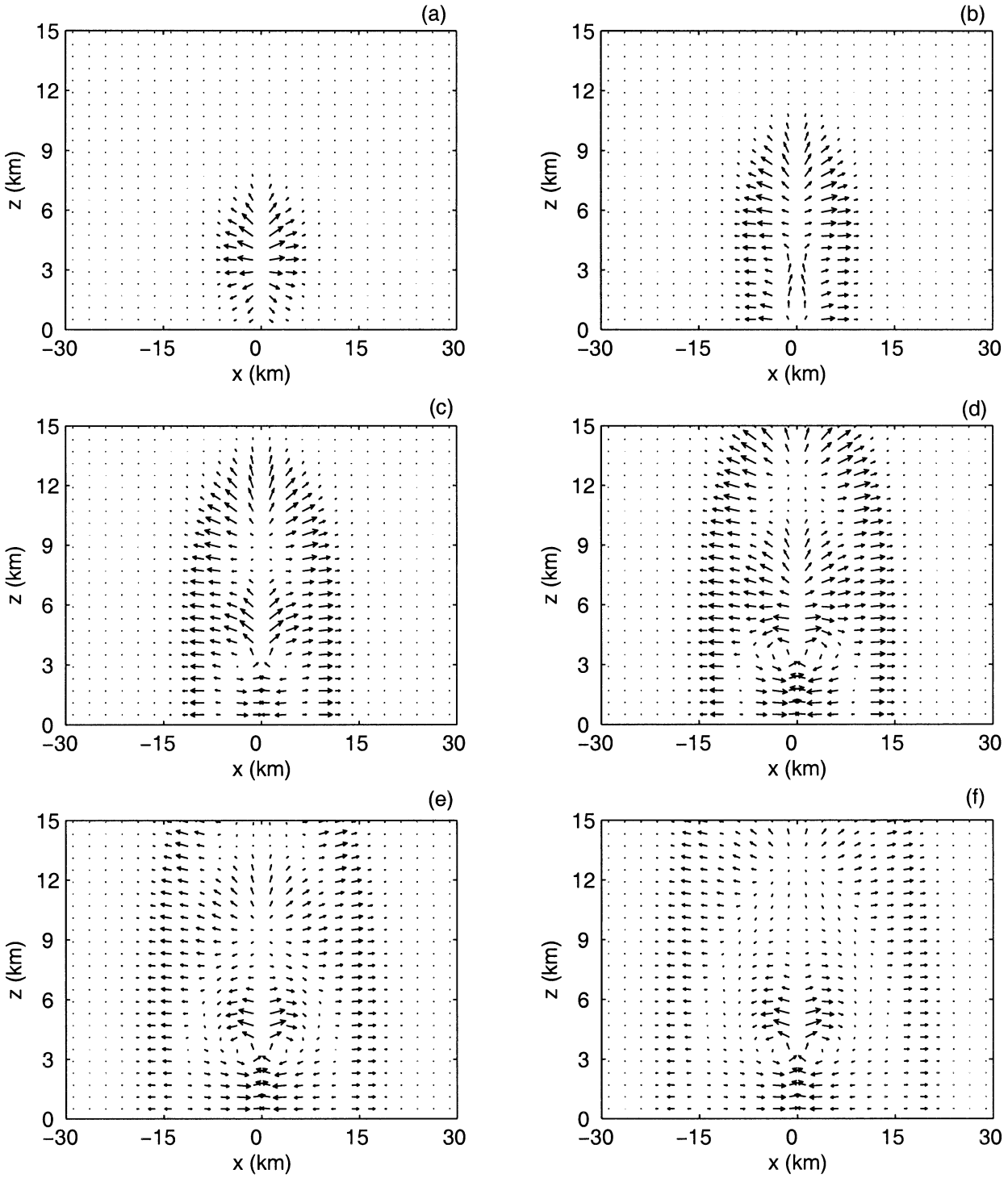

FIG. 4. Time-dependent displacement fields calculated over 10-s intervals ending (a) 10, (b) 20, (c) 30, (d) 40, (e) 50, and (f) 60 s following an impulsive heat injection. When the heating amplitude is 1 K, a head-to-tail length vector is 3.1 m (5.1 m) in the x (z) direction.

tively from the steady state of Bannon (1995) in that a low pressure perturbation exists below the heated region and is not yet strictly hydrostatically balanced at the end of the acoustic stage. Figure 5b demonstrates the horizontal propagation of the acoustic signal along the lower boundary (i.e., the Lamb wave). Because the heating is elevated, the signal appears along the lower boundary a few seconds following the heating. The wide signal that first appears on the lower boundary consists of some vertically propagating acoustic waves. After these

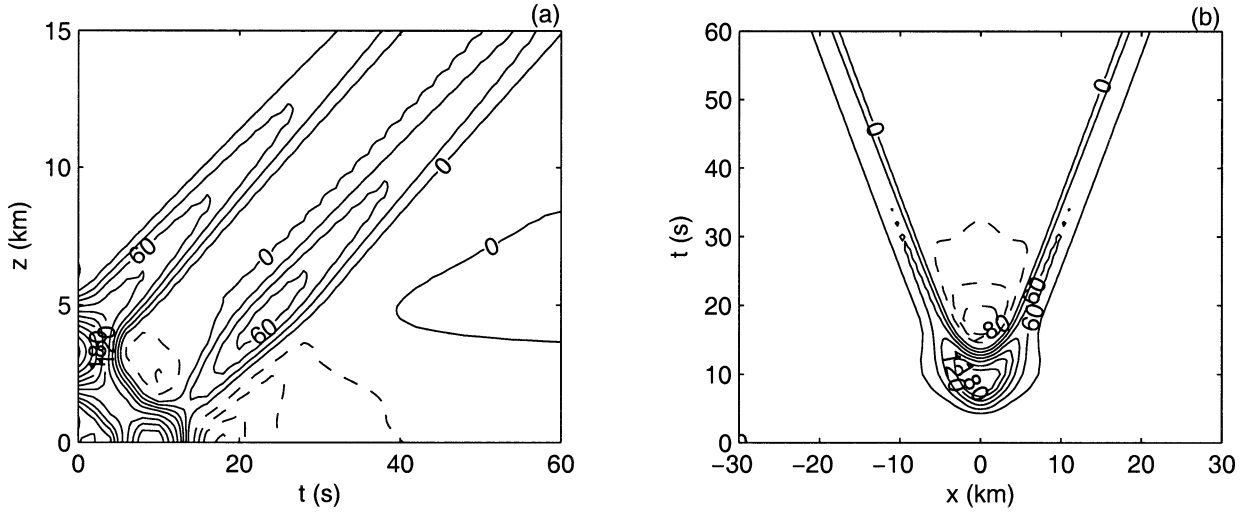

FIG. 5. Temporal cross section of the perturbation pressure field at (a) $x = 0$ as a function of height z and time t, and (b) at $z = 0$ as a function of distance x and time t following an impulsive heat injection. The heating depth and elevation are $d = 5$ km and $d_g = 1$ km with the peak heating occurring at $z = 3.5$ km. The contour interval is 20 Pa for $|p'| < 60$ Pa and 30 Pa otherwise. Here and elsewhere, negative contours are dashed.

waves have reflected off the lower boundary, the primary signal is the Lamb wave. In this two-dimensional problem, the acoustic wave signal decays as $t^{-1/2}$ (Lighthill 1978, his section 1.4). However, the Lamb wave signal is essentially one-dimensional and therefore must not exhibit any decay in order for its energy to be conserved. The one-dimensional Lamb wave group consists of a large, narrow positive perturbation, whereas the two-dimensional acoustic wave groups consist of the leading positive perturbation and trailing negative perturbation (Lighthill 1978, his Fig. 20). The negative perturbation trailing the Lamb wave in Fig. 5 is mainly due to a loss of mass in the heated column at the onset of the upper-level outflow and the buoyancy adjustment.

Figure 6 presents the time-dependent displacement field in the first 12 min following the heat injection. This stage of adjustment is dominated by the emergence of nonhydrostatic buoyancy waves. In the first minutes, these waves accomplish a net upward displacement of the heated layer accompanied by a pattern of inflow/outflow. This initial circulation is evident at the end of the acoustic stage (see Figs. 4e,f). By the 6th min an upper-level pattern of inflow is established and sinking takes place in the core of the heated column, and the circulation that initially developed on the periphery of the heated region is propagating away from the heated column. The interaction of the downward-propagating waves with the lower-boundary results in localized circulation patterns confined to the lower boundary. Figure 7 presents a refined view of these lower-boundary rotors as they propagate through the region marked A in Fig. 6 during the 6th to 12th minutes. The outflow associated with these rotors is approximately 4 km wide, 1 km deep, and propagates at a horizontal speed of approximately 15 m s^{-1}. The phase speed and scale of the rotors can be determined from the group speed and wavelength of the higher vertical wavenumber, vertically propagating gravity wave groups that interact with the rigid lower boundary in order to generate the rotors. The rotors displace the location of maximum horizontal convergence away from the heated core and elevate the inflow region.

Figure 8 presents cross sections of the potential temperature field during the nonhydrostatic buoyancy stage. Integration of the heat equation (2.1d) with respect to time demonstrates that the potential temperature perturbation depends on the time-integrated heating as well as the time-integrated advection of the base-state potential temperature. The time-integrated vertical advection is proportional to the net vertical displacement. Because the acoustic and Lamb waves do not produce very large vertical displacements whereas the buoyancy waves do produce large vertical displacements, the potential temperature perturbation effectively isolates the buoyancy waves. The shortest buoyancy period is $\tau_b = 2\pi/N_s \approx 324$ s, which corresponds to a wave with zero horizontal group velocity (i.e., Fig. 1 indicates that as the wave aspect m/k approaches zero, the slope of the dispersion curve in the buoyancy class approaches zero and the frequency approaches N_s). This oscillation is evident in Fig. 8a. After a period τ_b following the heat injection, the potential temperature perturbation is reduced by approximately 80%. The apparent negative vertical phase speed of these buoyancy waves is in contrast to the positive vertical phase speed of the acoustic waves in Fig. 5a. Recall that the direction of energy propagation (particle motions) and phase propagation are parallel in an acoustic wave, but are orthogonal for the buoyancy waves. Therefore, the negative vertical phase speed apparent in Fig. 8a does not imply the

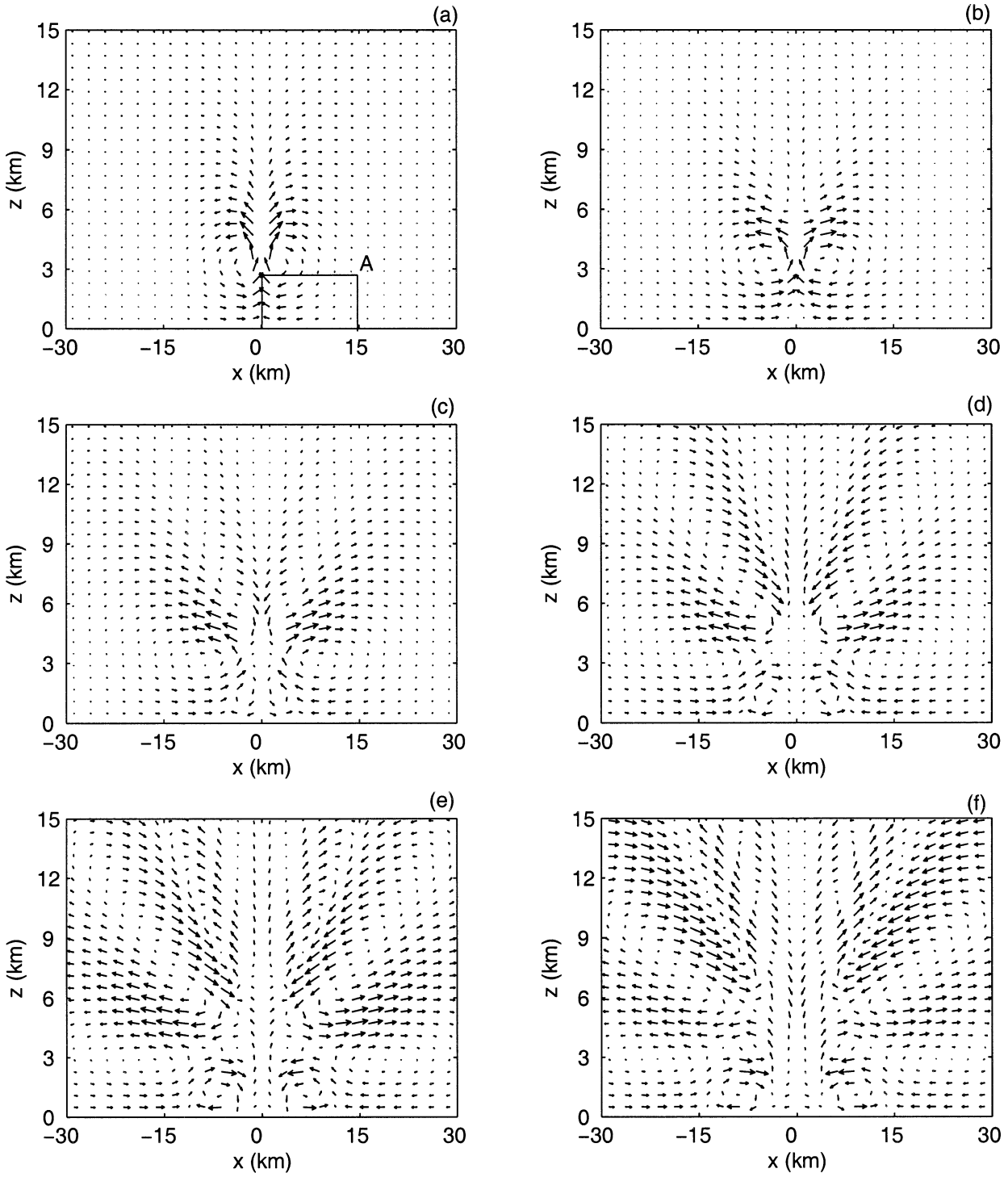

FIG. 6. Time-dependent displacement fields calculated over 2-min intervals ending (a) 2, (b) 4, (c) 6, (d) 8, (e) 10, and (f) 12 min following an impulsive heat injection. When the heating amplitude is 1 K, a head-to-tail length vector is 46.9 m (52.2 m) in the x (z) direction.

downward propagation of a signal. Rather some of the initial perturbation present at the left edge of Fig. 8a propagates upward and is responsible for the emergence of the perturbation aloft at 6 min. Figure 8b demonstrates the continued emergence of several wave groups from the heated region during the nonhydrostatic buoyancy stage. The waves slowest to emerge from the heated region are of increasing vertical wavenumber.

The distinction between the acoustic and buoyancy stages of adjustment is emphasized by examining ver-

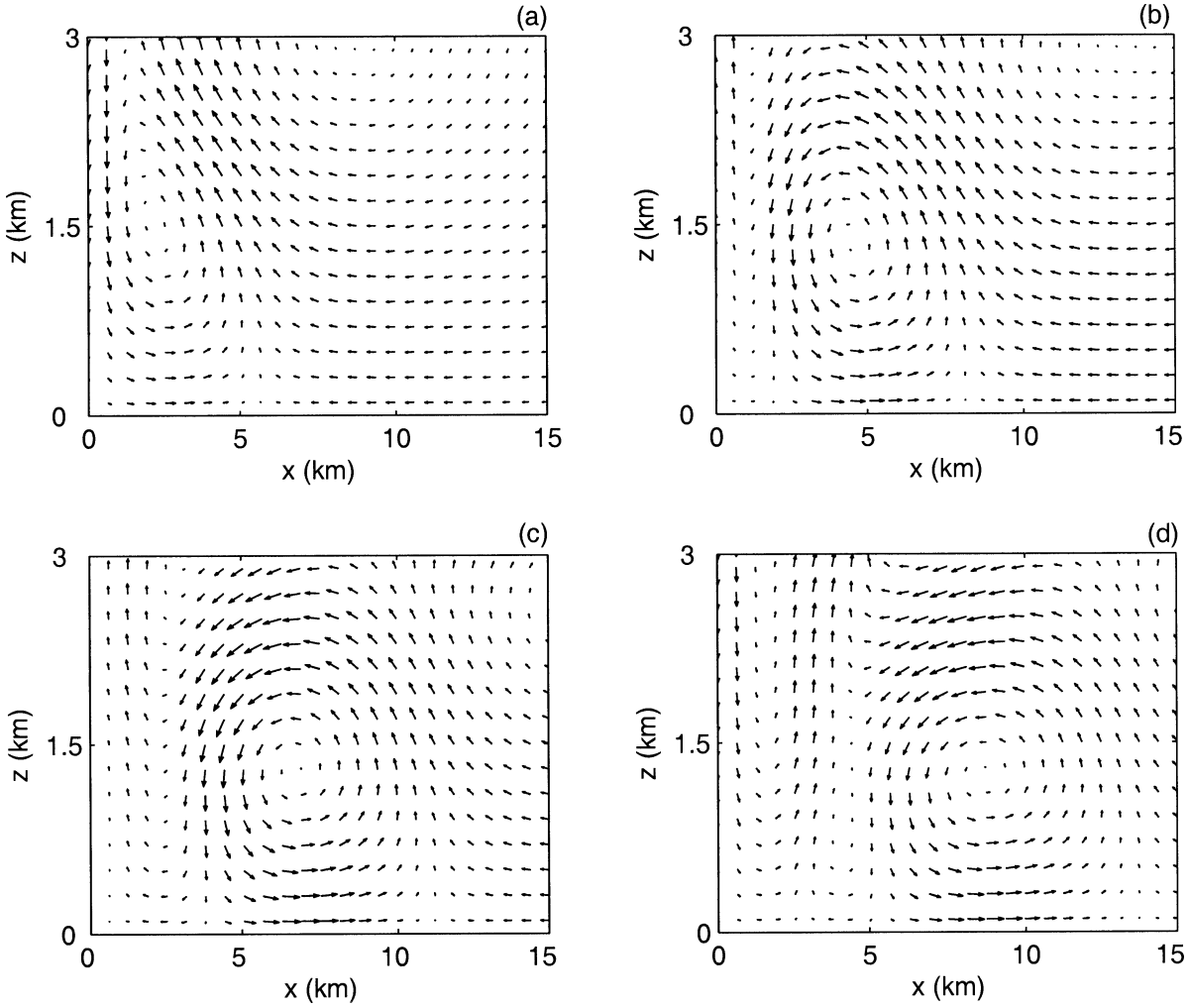

FIG. 7. Refined view of region A in Fig. 6a containing the outwardly propagating boundary rotor at times (a) 6, (b) 8, (c) 10, and (d) 12 min following an impulsive heating. A head-to-tail length vector is 23.5 m (26.1 m) in the x (z) direction.

tical profiles (Fig. 9) of parcel trajectories on the periphery of the heated regions. During the acoustic stage, air parcels are displaced outward from the heated region. Aloft, the magnitude of the displacements is a decreasing function of height. During the buoyancy stage, the displacements are an order of magnitude larger and exhibit more detail than during the acoustic stage. Initially, air parcels located below the level of midheating ($z = 3.5$ km) are drawn toward the heated column while those located aloft are pushed outward. At all levels below the top of the heating ($z < 6$ km) there is sinking. This is the signal associated with the lowest vertical wavenumber modes that are in phase with the heating, described by Bretherton and Smolarkiewicz (1989). The lower boundary constrains the ability of air parcels to accelerate downward in the vicinity of the boundary. Following the initial subsidence the air parcels accelerate upward toward their initial position, which they overshoot, and are subsequently accelerated downward. While this vertical oscillation occurs, air parcels located slightly above (below) the level of midheating continue moving outward (inward) horizontally. In the vicinity of the lower boundary (e.g., $z = 0.5$ km), air parcels that initially are drawn inward are accelerated outward by the lower-boundary rotors demonstrated in Fig. 7. Aloft ($z > 6$ km), air parcels oscillate both vertically and horizontally about their initial position with amplitude decreasing with increasing height. This decrease in amplitude with increasing distance from the heat source occurs because the energy density of the propagating two-dimensional buoyancy wave group decreases with increasing distance from the source.

b. Intermediate-scale heating (intermediate aspect ratio and duration)

In the second experiment, we let $a = 25$ km, $d = 9$ km, $d_g = 1$ km, and $\tau = 20$ min such that the aspect ratio is $\delta = 0.18$. Although the heating duration is much longer than an acoustic wave period, an acoustic ad-

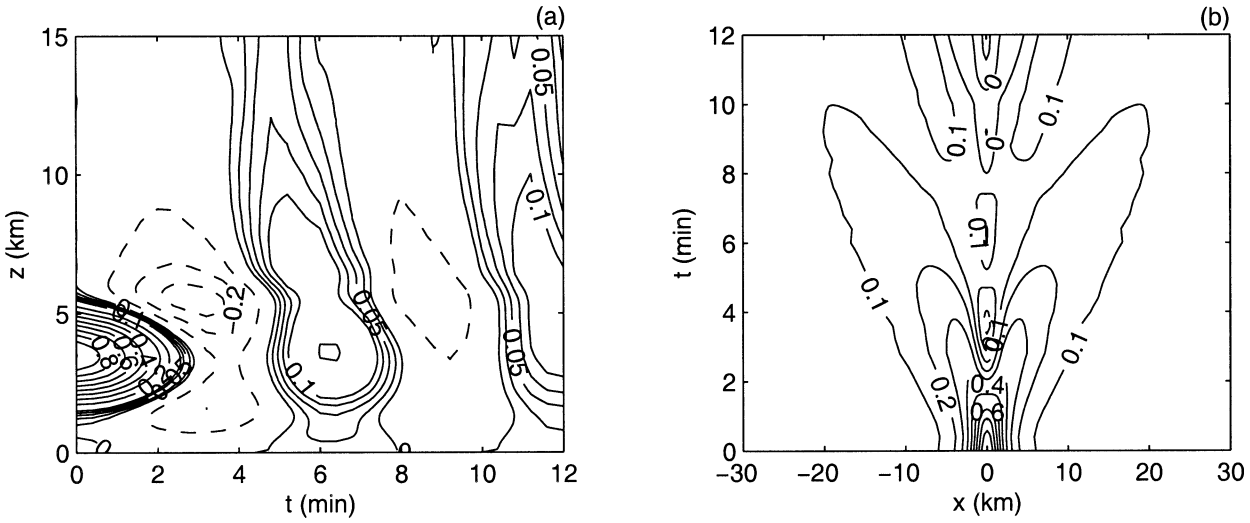

FIG. 8. Temporal cross section of the perturbation potential temperature field at (a) $x = 0$ as a function of height z and time t, and (b) at the level of midheating $z = 3.5$ km as a function of distance x and time t following an impulsive heat injection. The contour interval is 0.025 K for $|\theta'| < 0.1$ K and 0.1 K otherwise.

justment is still discernible in this experiment, as will be demonstrated. Such an injection models a large convective storm. The maximum pressure perturbation of 27 Pa is much smaller than that generated by the impulsive heating (307 Pa) despite the fact that the heating amplitude $\Delta\theta$ is the same.

Figure 10 presents time-dependent displacement vectors computed over 10-min intervals during the first hour following the onset of heating. The displacement field is dominated by the action of buoyancy waves. As in Fig. 6, the injection initially displaces the heated column upward and circulating patterns of inflow and outflow emerge on the periphery of the heated column. The lower-boundary rotors are again evidenced by the outward and upward displacement of the inflow region established initially beneath the heated core. The more complicated patterns of inflow and outflow that emerged above the heated region in the cumulus-scale experiment are still present in this experiment but of smaller magnitude relative to the lowest vertical wavenumber circulation. The vertical-to-horizontal aspect ratio of the displacements is approximately 0.1, which implies that

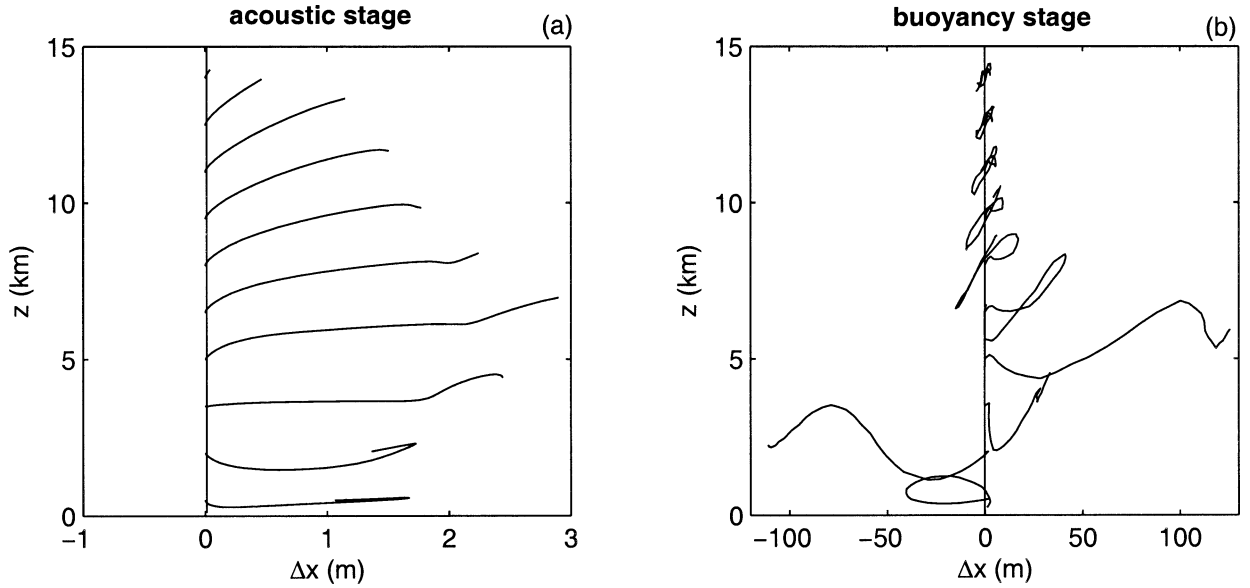

FIG. 9. Trajectories of parcels during (a) the first 30 s and (b) the first 12 min at heights between $z = 0.5$ km and $z = 11$ km and at a horizontal distance of 5 km east of the center of an impulsive heat injection of half-width $a = 2$ km, depth $d = 5$ km, elevation $d_g = 1$ km, and amplitude $\Delta\theta = 1$ K.

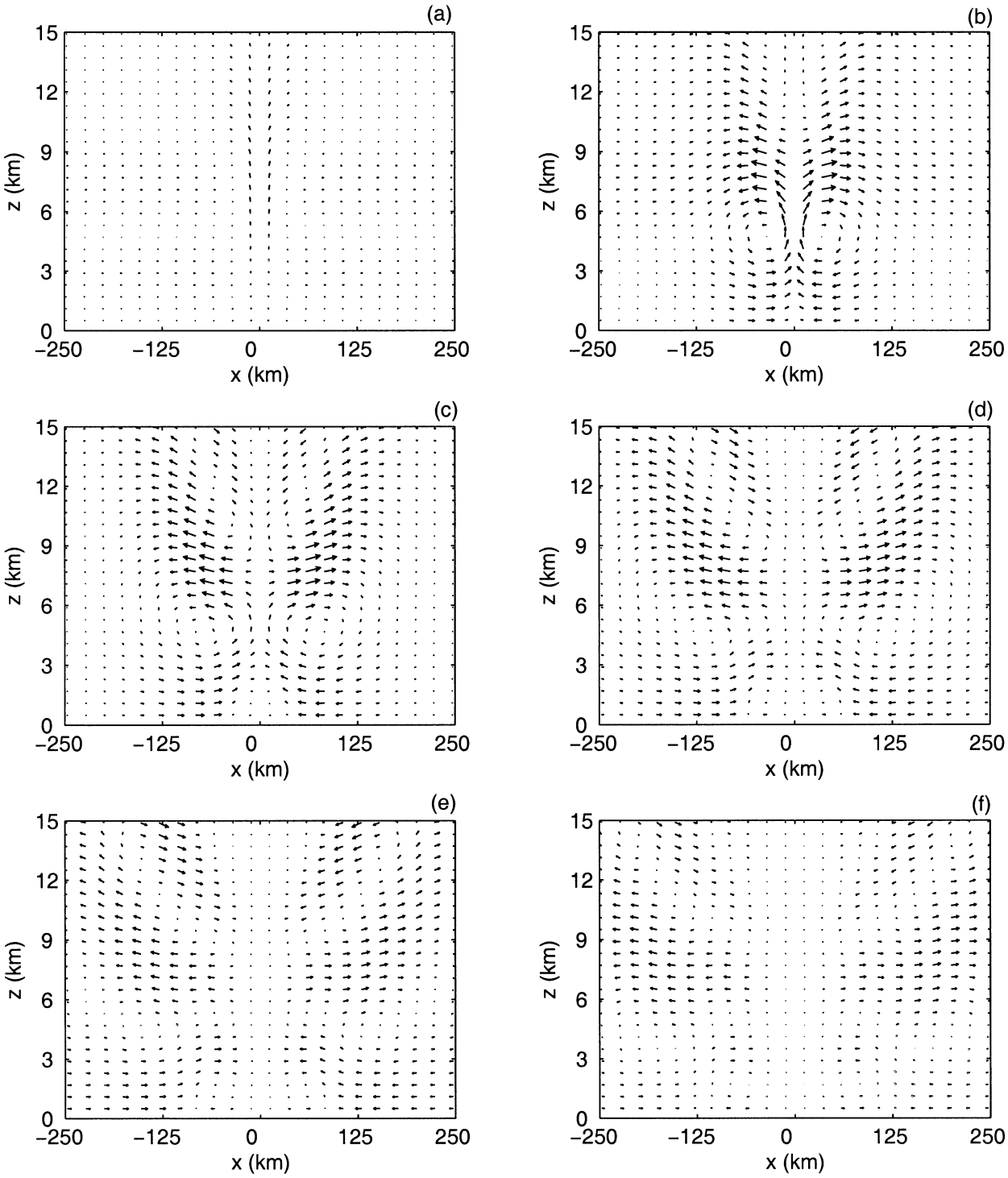

FIG. 10. Time-dependent displacement fields calculated over 10-min intervals ending (a) 10, (b) 20, (c) 30, (d) 40, (e) 50, and (f) 60 min following a heat injection of duration 20 min. When the heating amplitude is 1 K, a head-to-tail length vector is 312 m (39.7 m) in the x (z) direction.

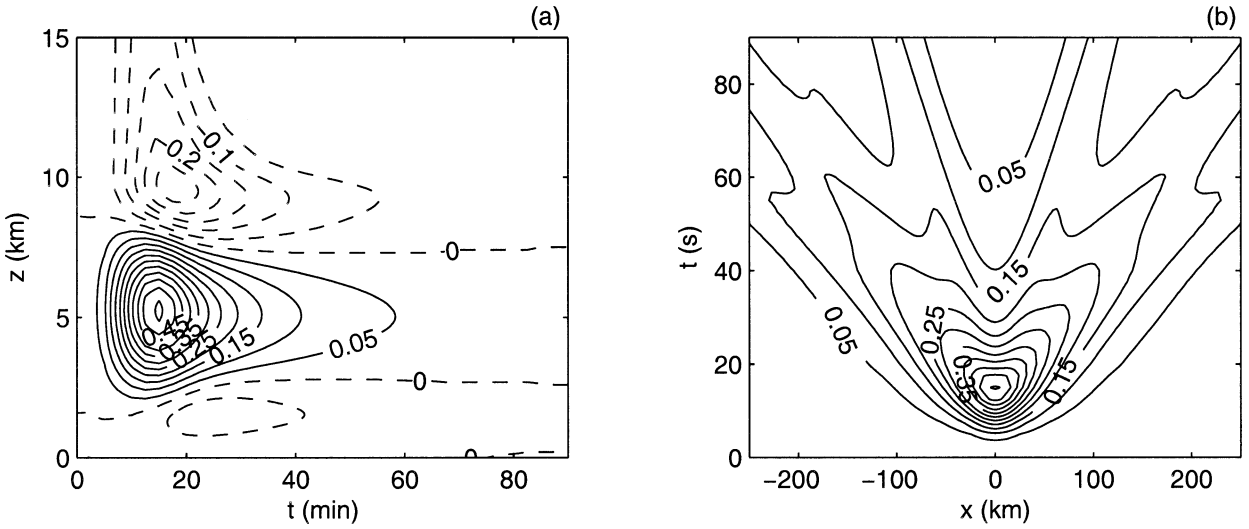

FIG. 11. Temporal cross section of the perturbation potential temperature field at (a) $x = 0$ as a function of height z and time t, and (b) at the level of midheating $z = 5.5$ km as a function of distance x and time t following a heat injection of duration 20 min. The contour interval is 0.05 K.

the dominant buoyancy waves are weakly nonhydrostatic. (Note: Our means for establishing what constitutes nonhydrostatic, weakly nonhydrostatic, and hydrostatic waves is arbitrary and is based on the vertical–horizontal aspect ratio of the particles displaced by the waves.) Vertical profiles of parcel trajectories along the periphery of the heated region resemble those presented in Fig. 9b except for an order of magnitude decrease in the trajectory aspect ratio.

Figure 11 presents temporal cross sections of the potential temperature field, similar to Fig. 8. The high-frequency buoyancy oscillations present in Fig. 8a are not present in Fig. 11a. These oscillations are not generated significantly by such long-duration injection. The regions of negative perturbation that emerge both above and below the heated layer indicate upward vertical displacement (i.e, the advection of lower base-state values of potential temperature). This vertical advection limits the maximum amplitude of the potential temperature perturbation to ~0.55 K. Within 20 min of the cessation of heat injection, these anomalies are removed by the propagation of buoyancy waves. Figure 11b demonstrates the emergence of these waves from a location in the middle of the heated layer. The dispersive nature of the waves leads to a decay in the amplitude of these signals of more than 80% after they have propagated 200 km away from the heated region. Once again, the hydrostatic and geostrophic steady state towards which this atmosphere adjusts is approximately trivial (i.e., the perturbations in the asymptotic steady state are negligible compared to the initial and transient perturbations).

Figure 12a demonstrates the evolution of the vertical profile of pressure at $x = 0$ during the injection of heat. Vertically propagating acoustic waves are not evident as they were in Fig. 5a. Rather, a deep region of positive pressure perturbation emerges smoothly above and throughout most of the heated region. The positive perturbation is mainly a hydrostatic contribution from the net upward expansion of the column. The negative perturbation along the lower boundary indicates the loss of mass from the column due to upper-level outflow. Figure 12b demonstrates the evolution of the horizontal profile of pressure along the lower boundary. Although the displacement field is dominated by buoyancy wave motions and the heating duration is longer than the acoustic wave period, a discernible Lamb wave signal emerges from the heated layer and propagates horizontally. Unlike that in Fig. 5b, the amplitude of the Lamb wave signal increases in time. This amplification is the result of the accumulation of continuously generated Lamb waves during the application of the finite-duration heating.

c. *Mesoscale heating (shallow aspect ratio, long duration)*

In the third experiment, we let $a = 100$ km, $d = 9$ km, $d_g = 1$ km, and $\tau = 2$ h such that the aspect ratio is $\delta = 0.045$. Here the heating duration is longer than a typical nonhydrostatic buoyancy wave period. Such an injection is intended to model a large organized mesoscale convective system. While the individual convective elements that comprise such a system are likely to excite a wave response similar to those presented above, a response to the conglomerate system by the larger synoptic-scale environment is likely to involve hydrostatic, rotating buoyancy waves, and a nontrivial hydrostatic and geostrophic steady state.

The time-dependent displacement vectors are omitted for this experiment because they resemble qualitatively those in Fig. 10 except on longer time and larger hor-

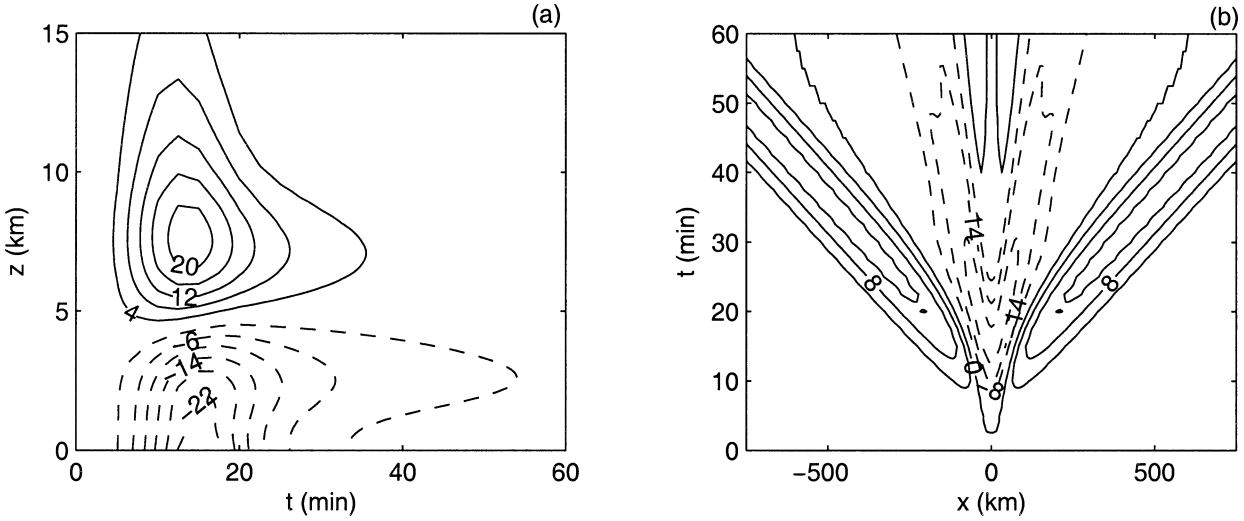

FIG. 12. Temporal cross section of the perturbation pressure field at (a) $x = 0$ as a function of height z and time t, and (b) at $z = 0$ as a function of distance x and time t following a heat injection of duration 20 min. The contour interval is (a) 4 Pa and (b) 4 Pa for $|p'| <$ 12 Pa and 8 Pa otherwise.

izontal spatial scales with maximum horizontal and vertical displacements $\Delta x = O(1\text{ km})$ and $\Delta z = O(10\text{ m})$. The aspect ratio of these displacements is approximately 0.01 and the time scale of the transients is an order of magnitude longer than the maximum buoyancy wave period. These two conditions imply that the transients are approximately hydrostatic. The adjustment to the conglomerate system is therefore accomplished primarily by hydrostatic buoyancy waves.

Figure 13 presents temporal cross sections of the potential temperature field, similar to Figs. 8 and 11. Unlike the previous two experiments, the potential temperature perturbation adjusts toward a nontrivial geostrophic and hydrostatic state. After approximately 6 h the perturbation at $z = 0$ is comprised of this steady state and inertia-gravity waves. The steady state qualitatively resembles the solutions presented in Chagnon and Bannon (2001). The lowest frequency waves form an inertial oscillation of maximum period $2\pi/f \approx 17.4$ h.

In spite of the long duration and large horizontal scale of this injection, a Lamb wave signal is again discernible. Figure 14 presents temporal cross sections of the pressure perturbation in the first 4 h following the onset of heat injection. The magnitude of the Lamb signal is similar to that in the previous experiment. The primary difference is in the width of the signal, which is determined by the duration and width of the injection. The sharpness of the leading and trailing edges of the Lamb signal is determined by the time scale associated with the start-up and shutoff of the heat injection (4.1). To illustrate this, we replace the temporally smooth sine-squared heating in (4.1) with one that is a top-hat in

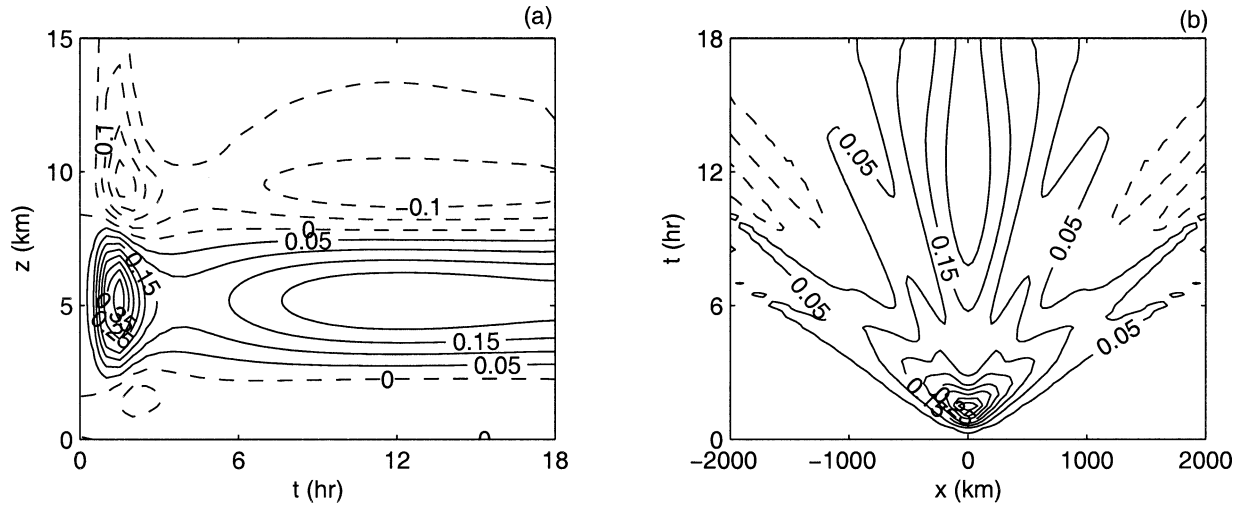

FIG. 13. As in Fig. 11 except following a heat injection of duration 2 h.

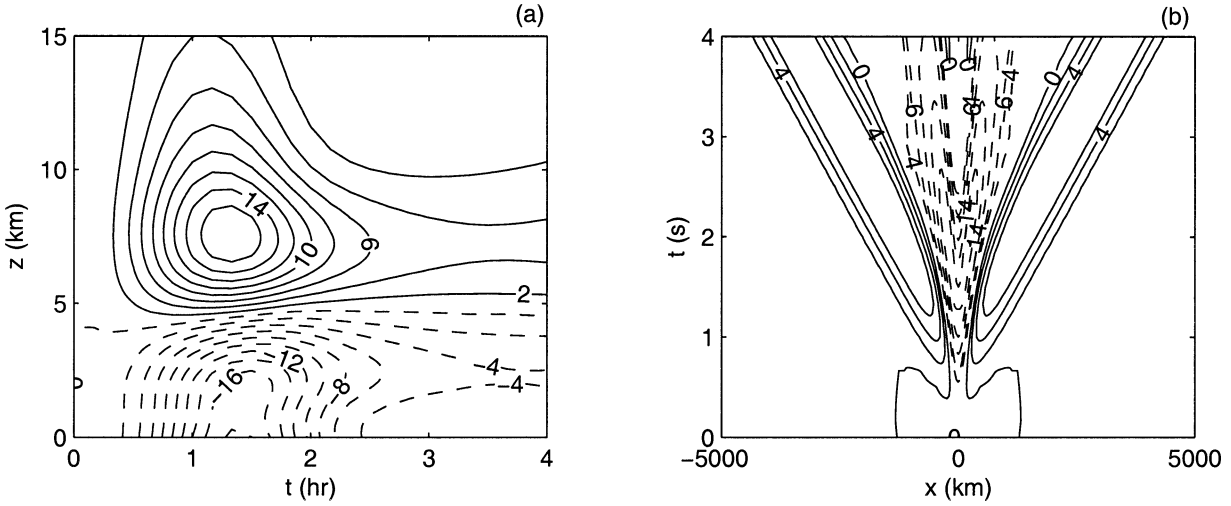

FIG. 14. As in Fig. 12 except following a heat injection of duration 2 h. The contour interval is (a) 2 Pa and (b) 2 Pa for $|p'| < 12$ Pa and 4 Pa otherwise.

time (of identical time-integrated amplitude). Figure 15 presents the temporal cross sections of pressure following this ''sharper'' heat injection. The leading and trailing edges of the Lamb wave signal in Fig. 15b are indeed more abrupt than those generated by the sine-squared injection (see Fig. 14b). Figure 15a demonstrates that the sudden shutoff produces a rapid decrease in the amplitude of the profile at $z = 0$ at $t = 2$ h. This indicates an acoustic adjustment accomplished by the Lamb waves and is an example of the presence of multiple time scales associated with the higher-order derivatives of the injection.

5. Summary

This paper presents an analytic investigation of hydrostatic and geostrophic adjustment. A fully compressible linear model is solved subject to an external injection of mass, momentum, or heat. Specific solutions were demonstrated only for the case of an external heating. The injection is intended to model the net effect of processes with characteristic scales smaller than those on which the linear model is justifiable. The spatial structure of solutions is described by a set of basis functions satisfying the rigid lower-boundary condition. One such structure is the Lamb mode that decays exponentially from the lower boundary. This mode contains only the pressure and horizontal velocity components. Because the rigid lower-boundary condition is of a different form for the vertical velocity and pressure fields, there are two sets of basis functions describing the solution state.

The time-dependence of each spatial mode is generalized in terms of a temporal Green's function. This func-

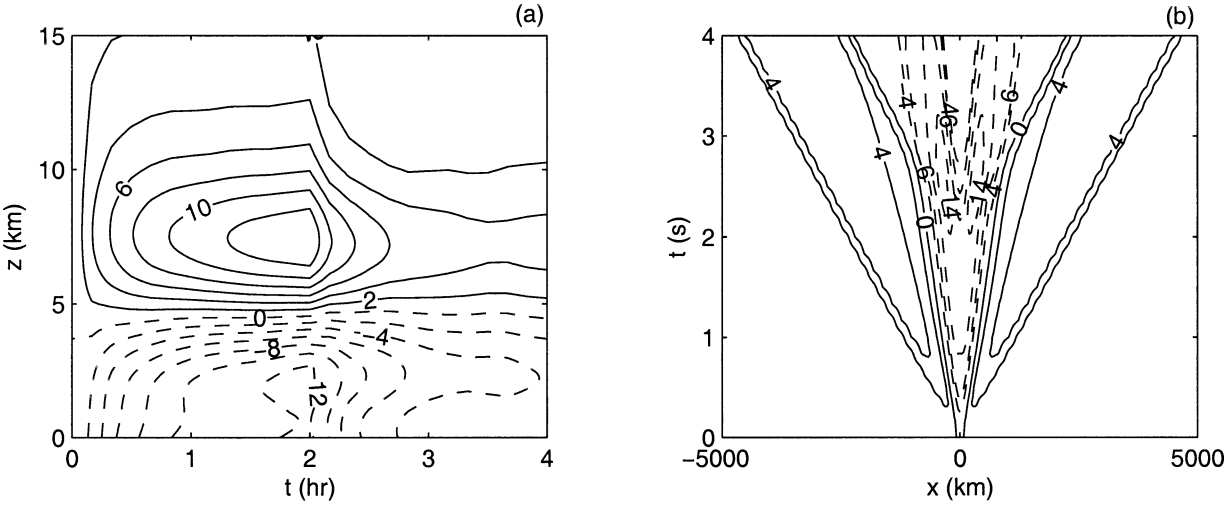

FIG. 15. As in Fig. 14 except following a top-hat injection of heat.

tion resembles a solution to the homogeneous problem, which is solved as an eigenvalue–eigenvector problem. The eigenvalues correspond to steady, acoustic wave, and buoyancy wave classes. The exception is the Lamb mode, which contains only a steady and an acoustic class. When the heating is of finite duration, the time-dependence of each spatial mode may still be written as a sum of these distinct time-dependencies except that the projections onto each of these classes are time dependent.

Some basic properties of the adjustment process are demonstrated by considering a localized injection of heat. The heating considered in this paper is invariant in the *y* direction. The response is therefore also two-dimensional, which implies that the amplitude of disturbances generated by the heating will decay more slowly with distance than in the general three-dimensional adjustment problem. The comparison of adjustment to two-dimensional heat injection of varying spatial and temporal scales reveals the existence of several regimes comprising the adjustment. Here, we summarize the qualitative aspects of these regimes.

An instantaneous heat injection generates acoustic waves, which are primarily responsible for accomplishing an expansion of the heated region. With the exception of the Lamb wave, acoustic waves are not excited by heating of duration exceeding several minutes. Though much diminished in amplitude, the Lamb wave may be generated by heating of a duration of several hours provided the horizontal scale is large. The parcel displacements associated with the acoustic waves are small relative to the buoyancy waves, though the pressure perturbation may be quite large.

An instantaneous heat injection also generates nonhydrostatic buoyancy waves, provided the vertical–horizontal aspect ratio is not very small. Such waves propagate much of their energy vertically and can accomplish a large vertical displacement of the heated column. The lowest vertical wavenumber modes have the largest horizontal group speed and are the first to emerge from the heated region. These waves consist of a leading group of negative vertical velocity perturbation, trailed by a positive potential temperature perturbation that is in phase with the heating. Furthermore, the leading group is accompanied by a pattern of upper-(lower)-level outflow/inflow. Bretherton and Smolarkiewicz (1989) identify this signal as that required to remove the buoyancy excess associated with the cloud. As higher vertical wavenumber modes emerge slowly from the cloud, more complicated patterns of inflow and outflow are established both aloft and along the lower boundary. Chagnon and Bannon (2001) demonstrate that the lowest vertical wavenumber pattern contributes most significantly to the total displacement required to establish a balanced state. This balanced state is approximately trivial when the horizontal scale of the heating is very small compared to the Rossby deformation radius, which is $O(1000$ km) for these experiments.

When the duration of heat injection is extended to 20 min and the aspect ratio is decreased to $\delta = 0.18$ the transient motions are only weakly nonhydrostatic and occur on time scales longer than the shortest buoyancy period. Within 2 h the transients disperse from the heated region leaving behind an approximately trivial balanced state. When the duration is extended to 2 h and the aspect ratio is decreased to $\delta = 0.045$, the transient response involves only low-frequency, hydrostatic buoyancy waves. After several hours the only transients remaining in the vicinity of the heated region are inertia-gravity waves oscillating slowly about a nontrivial balanced state.

The evolution of the inflow region beneath the heated core has some interesting properties. Following the initial upward displacement of the heated core and the onset of inflow, horizontally propagating rotors emerge along the lower boundary. The rotors result from the interaction of downward-propagating buoyancy waves with the lower boundary. The velocity field associated with these rotors is directed opposite to the inflow and forces an outward and upward displacement of the inflow layer. Because the low-level inflow is believed to be essential to the self-aggregating properties of convective systems via the wave-CISK (conditional instability of the second kind) mechanism (Lindzen 1974; Raymond 1976), these lower-boundary rotors could play a significant role in the evolution of organized cloud clusters.

Lamb's (1932) problem considered the vertical adjustment by a compressible atmosphere to horizontally invariant perturbations. The numerous recent extensions of Lamb's problem (Bannon 1995; Sotack and Bannon 1999; Kalashnik 2000; Duffy 2003) offer a theory to explain how an atmosphere establishes and maintains hydrostatic balance. Essentially, a warmed compressible atmosphere must expand vertically in order to establish hydrostatic balance. If the perturbation is introduced rapidly, then acoustic waves will provide most of the necessary displacement. The solution presented in this paper places this theory in the more general context of vertical and horizontal adjustment. Strictly, Lamb's hydrostatic adjustment by acoustic waves explains only the horizontal wavenumber-0 response. Nonhydrostatic buoyancy waves account for much of the adjustment when the injection aspect ratio is large. The time scale of these waves, and hence the time scale of hydrostatic adjustment, may be an order of magnitude longer than the vertical acoustic adjustment. Furthermore, the acoustic adjustment is not confined to the vertical. The presence of a rigid lower boundary requires an increase/decrease in pressure throughout the depth of the atmosphere when the column attempts to expand/contract against the fixed lower boundary. This signal is communicated horizontally by the Lamb waves.

Any small set of experiments, such as those presented here, cannot adequately explore the vast parameter space describing the detail of the injection. The experiments involving a localized heat injection shown in this paper describe the basic dynamics of adjustment. However, a

broader perspective of the relationship between the details of the injection and the response may be obtained by considering the potential vorticity distribution and energetics of these solutions. In the second part of this study, we examine these issues.

Acknowledgments. Professor Sabih Hayek provided insightful advice for improving the mathematical analysis. The insight of Professors Sukyoung Lee and John H. E. Clark as well as the three anonymous reviewers was invaluable to the preparation of this manuscript. Partial financial support was provided by the National Science Foundation under NSF Grants ATM-9521299, ATM-9820233, and ATM-0215358.

APPENDIX

Coefficients of the Temporal Green's Function

Section 3b generalizes the forced solutions in terms of a temporal Green's function. The Green's function is of the form $\hat{\boldsymbol{\chi}}_n = \mathbf{E}_n \boldsymbol{\psi}_n$, where the eigenvector matrix $\mathbf{E}_n$ and the vector of time dependencies $\boldsymbol{\psi}_n$ are provided in (3.9). Recall that the external injection vector of the Green's function solution is denoted by $\hat{\mathbf{F}}_n^{\mathrm{T}} = \delta(t)\sigma_k(s_1, s_2, s_3, s_4, s_5)_n$. Conditions on the coefficients C_i of the temporal Green's function are given by (3.14), which may be written as the linear algebraic system $\mathbf{E}_n\mathbf{C}_n = \mathbf{F}_n^o$ where the ith element of $\mathbf{C}_n$ is C_i and the ith element of the temporally integrated injection function, $\mathbf{F}_n^o$, is $F_i^o = \sigma_k s_i$. For the specific solutions demonstrated in section 4, all elements of $\mathbf{F}_n^o$ are zero except for the contribution from the heating, $F_4^o = \sigma_k s_4$. Nonetheless, we present the solution for general case of nonzero elements throughout $\mathbf{F}_n^o$, as these solutions will be demonstrated in a future investigation. Solving for the coefficients C_i involves inverting $\mathbf{E}_n$, the result of which is complicated and not obviously meaningful. Rather than explicitly provide $\mathbf{E}_n^{-1}$, we provide only the explicit solution for the coefficients C_i:

$$C_1 = \frac{gf}{\omega_a\omega_b\xi}\left\{F_2^o(B_{42} - B_{44}) + F_4^o(B_{24} - B_{22}) + F_5^o\left[E_{21}(B_{42} - B_{44}) + E_{41}(B_{22} - B_{24}) + \frac{\omega_a\omega_b\xi}{gf}\right]\right\}, \tag{A.1}$$

$$C_3 = \frac{1}{2\xi}\left[F_1^oE_{34} + F_2^o\frac{gf}{\omega_a\omega_b}B_{44} - F_3^oE_{14} - F_4^o\frac{gf}{\omega_a\omega_b}B_{24} + F_5^o\frac{gf}{\omega_a\omega_b}(B_{24}E_{41} - B_{44}E_{21})\right], \tag{A.2}$$

$$C_3 = \frac{1}{2\xi}\left[-F_1^oE_{34} + F_2^o\frac{gf}{\omega_a\omega_b}B_{44} + F_3^oE_{14} - F_4^o\frac{gf}{\omega_a\omega_b}B_{24} + F_5^o\frac{gf}{\omega_a\omega_b}(B_{24}E_{41} - B_{44}E_{21})\right], \tag{A.3}$$

$$C_4 = \frac{1}{2\xi}\left[-F_1^oE_{32} - F_2^o\frac{gf}{\omega_a\omega_b}B_{42} + F_3^oE_{12} + F_4^o\frac{gf}{\omega_a\omega_b}B_{22} + F_5^o\frac{gf}{\omega_a\omega_b}(D_{42}E_{21} - B_{22}E_{41})\right], \tag{A.4}$$

$$C_5 = \frac{1}{2\xi}\left[F_1^oE_{32} - F_2^o\frac{gf}{\omega_a\omega_b}B_{42} - F_3^oE_{12} + F_4^o\frac{gf}{\omega_a\omega_b}B_{22} + F_5^o\frac{gf}{\omega_a\omega_b}(B_{42}E_{21} - B_{22}E_{41})\right], \tag{A.5}$$

where E_{ij} represent the elements of the eigenvector matrix $\mathbf{E}_n$, and

$$\xi = \frac{ik\omega_a\omega_b(N_s^2 - f^2)(\omega_b^2 - \omega_a^2)}{(N_s^2 - \omega_a^2)(N_s^2 - \omega_b^2)(f^2 - \omega_a^2)(f^2 - \omega_b^2)}, \quad \text{and}$$

$$B_{22} = E_{22} - E_{21}, \qquad B_{24} = E_{24} - E_{21},$$

$$B_{42} = E_{42} - E_{41}, \quad \text{and} \quad B_{44} = E_{44} - E_{41}.$$

REFERENCES

Arfken, G., 1970: *Mathematical Methods for Physicists.* Academic Press, 815 pp.

Bannon, P. R., 1995: Hydrostatic adjustment: Lamb's problem. *J. Atmos. Sci.*, **52,** 1743–1752.

Blumen, W., 1972: Geostrophic adjustment. *Rev. Geophys. Space Phys.*, **10,** 485–528.

Bretherton, C. S., and P. K. Smolarkiewicz, 1989: Gravity waves, compensating subsidence and detrainment around cumulus clouds. *J. Atmos. Sci.*, **46,** 740–759.

Bryan, G. H., and J. M. Fritsch, 2002: A benchmark simulation for moist nonhydrostatic numerical models. *Mon. Wea. Rev.*, **130,** 2917–2928.

Chagnon, J. M., and P. R. Bannon, 2001: Hydrostatic and geostrophic adjustment in a compressible atmosphere: Initial response and final equilibrium to an instantaneous localized heating. *J. Atmos. Sci.*, **58,** 3776–3792.

——, and ——, 2005: Wave response during hydrostatic and geostrophic adjustment. Part II: Potential vorticity conservation and energy partitioning. *J. Atmos. Sci.*, **62,** 1330–1345.

Duffy, D. G., 2003: Hydrostatic adjustment of nonisothermal atmospheres. *J. Atmos. Sci.*, **60,** 339–353.

Eckart, C., 1960: *Hydrodynamics of Oceans and Atmospheres.* Pergamon Press, 290 pp.

Fritts, D. C., and L. Yuan, 1989: An analysis of gravity wave ducting in the atmosphere: Eckart's resonances in thermal and Doppler ducts. *J. Geophys. Res.*, **94,** 455–466.

Gill, A. E., 1982: *Atmosphere–Ocean Dynamics.* Academic Press, 662 pp.

Holton, J. R., 1983: The influence of gravity wave breaking on the general circulation of the middle atmosphere. *J. Atmos. Sci.,* **40,** 2497–2507.

——, J. H. Beers, and X. Zhou, 2002: On the vertical scale of gravity waves excited by localized thermal injection. *J. Atmos. Sci.,* **59,** 2019–2023.

Iga, K., 2001: Transition modes in stratified compressible fluids. *Fluid Dyn. Res.,* **28,** 465–486.

Kalashnik, M. M., 2000: Hydrostatic adjustment theory. *Izv. Atmos. Oceanic Phys.,* **36,** 203–209.

Lamb, H., 1932: *Hydrodynamics.* Dover, 738 pp.

Lighthill, J., 1978: *Waves in Fluids.* Cambridge University Press, 504 pp.

Lin, Y. L., and R. B. Smith, 1986: Transient dynamics of airflow near a local heat source. *J. Atmos. Sci.,* **43,** 40–49.

Lindzen, R. S., 1974: Wave-CISK in the tropics. *J. Atmos. Sci.,* **31,** 156–179.

Nicholls, M. E., and R. A. Pielke Sr., 2000: Thermally induced compression waves and gravity waves generated by convective storms. *J. Atmos. Sci.,* **57,** 3251–3271.

Obukhov, A. M., 1949: On the question of geostrophic wind. *Bull. USSR Acad. Sci.,* **13,** 281–306. (Translated from Russian by J. G. Howcroft.)

Raymond, D. J., 1976: Wave-CISK and convective mesosystems. *J. Atmos. Sci.,* **33,** 2392–2398.

——, 1986: Prescribed heating of a stratified atmosphere as a model for moist convection. *J. Atmos. Sci.,* **43,** 1101–1111.

Rossby, C.-G., 1937: On the mutual adjustment of pressure and velocity distributions in certain simple current systems, 1. *J. Mar. Res.,* **1,** 15–28.

——, 1938: On the mutual adjustment of pressure and velocity distributions in certain simple current systems, 2. *J. Mar. Res.,* **2,** 239–263.

Shutts, G., 1994: The adjustment of a rotating, stratified fluid to localized sources of mass. *Quart. J. Roy. Meteor. Soc.,* **120,** 361–386.

Sotack, T., and P. R. Bannon, 1999: Lamb's hydrostatic adjustment for heating of finite duration. *J. Atmos. Sci.,* **56,** 71–81.

Vadas, S. L., and D. C. Fritts, 2001: Gravity wave radiation and mean responses to local body forces in the atmosphere. *J. Atmos. Sci.,* **58,** 2249–2279.